

## Carbon fiber reinforced liquid crystalline elastomer composites: a dual exploration in strength augmentation and transformation flexibility through 4D printing

Yuliang Xia, Tong Mu, Yanju Liu & Jinsong Leng

To cite this article: Yuliang Xia, Tong Mu, Yanju Liu & Jinsong Leng (2024) Carbon fiber reinforced liquid crystalline elastomer composites: a dual exploration in strength augmentation and transformation flexibility through 4D printing, International Journal of Smart and Nano Materials, 15:2, 312-329, DOI: [10.1080/19475411.2024.2332645](https://doi.org/10.1080/19475411.2024.2332645)

To link to this article: <https://doi.org/10.1080/19475411.2024.2332645>



© 2024 The Author(s). Published by Informa UK Limited, trading as Taylor & Francis Group.



Published online: 29 Mar 2024.



Submit your article to this journal [↗](#)



Article views: 706



View related articles [↗](#)



View Crossmark data [↗](#)

# Carbon fiber reinforced liquid crystalline elastomer composites: a dual exploration in strength augmentation and transformation flexibility through 4D printing

Yuliang Xia<sup>a\*</sup>, Tong Mu<sup>a\*</sup>, Yanju Liu<sup>b</sup> and Jinsong Leng <sup>a</sup>

<sup>a</sup>Centre for Composite Materials and Structures, Harbin Institute of Technology (HIT), Harbin, People's Republic of China; <sup>b</sup>Department of Astronautical Science and Mechanics, Harbin Institute of Technology (HIT), Harbin, People's Republic of China

## ABSTRACT



Liquid Crystal Elastomers (LCEs) are renowned for their reversible deformation capabilities. Yet, enhancing their mechanical strength while retaining such flexibility has posed a considerable challenge. To overcome this, we utilized 4D printing to develop an innovative composite of LCE with carbon fiber fabric (LCEC). This approach has notably increased the tensile strength of LCE by eightfold, all the while maintaining its exceptional capacity for reversible deformation. By adjusting the alignment angle between carbon fiber and the LCE printing direction from 0° to 90°, the LCEC demonstrates an array of new deformation patterns, including bending, twisting, wrapping, and S-shaped transformations, which are distinct from pure LCE materials. Our study unveils that LCE composites exhibit deformation processes markedly different from their pure material counterparts, with the ability of pure LCE to sustain tensile strains exceeding 1900%. These findings, previously undocumented and unexplored, represent a substantial contribution to the field of smart materials. Employing finite element analysis, we explored the carbon fiber and LCE matrix dynamics, revealing bending mechanics in LCECs. This combined experimental and simulation approach yields crucial insights for crafting durable, high-strength LCECs with diverse deformational properties, advancing smart material technology.

## ARTICLE HISTORY

Received 30 November 2023  
Accepted 13 March 2024

## KEYWORDS

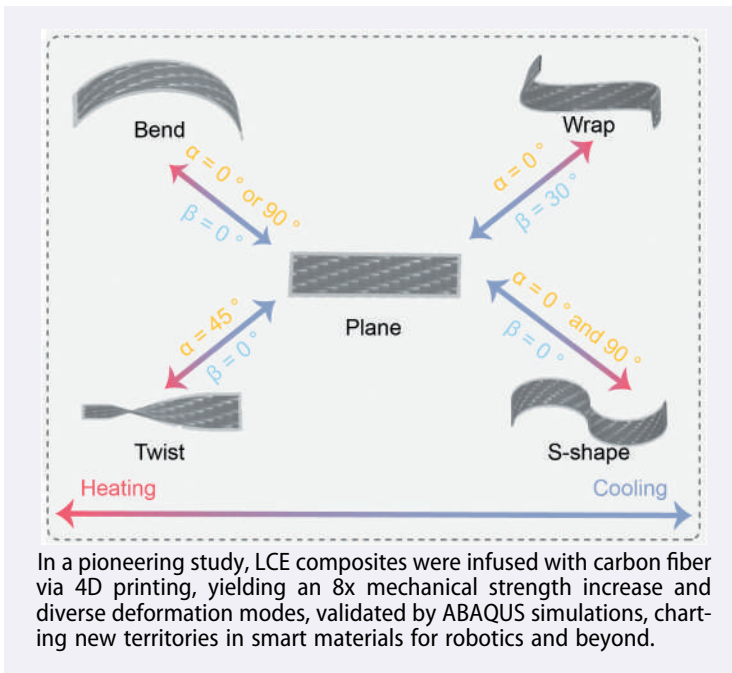
Liquid crystal elastomer composites; 4D printing; Smart materials

**CONTACT** Jinsong Leng  [lengjs@hit.edu.cn](mailto:lengjs@hit.edu.cn)  Department of Astronautical Science and Mechanics, Harbin Institute of Technology (HIT), No. 92 West Dazhi Street, Harbin 150001, People's Republic of China

\*These authors contributed equally to this work.

© 2024 The Author(s). Published by Informa UK Limited, trading as Taylor & Francis Group.

This is an Open Access article distributed under the terms of the Creative Commons Attribution License (<http://creativecommons.org/licenses/by/4.0/>), which permits unrestricted use, distribution, and reproduction in any medium, provided the original work is properly cited. The terms on which this article has been published allow the posting of the Accepted Manuscript in a repository by the author(s) or with their consent.



## 1. Introduction

LCEs embody a unique group of materials which amalgamate the properties of liquid crystals and elastomers [1–7]. Renowned for their responsive behavior, these materials undergo ordered phase transitions that can be triggered by a variety of environmental triggers, including thermal, photonic, or electrical inputs [8–12]. Consequently, this ability to adapt and change in response to their environment has rendered LCEs particularly attractive for a range of applications, spanning from adaptive optics to soft robotics and even biomedical devices [13–17]. Their deformability nature provides promising avenues for the creation of adaptive and ‘smart’ structures. Nevertheless, as with many novel materials, LCEs are not without their drawbacks. A significant challenge that persists with LCEs is their inherent low mechanical strength. While they can demonstrate remarkable reversible deformations, their mechanical properties often fall short, limiting their potential in load-bearing or mechanically demanding applications. This limitation stands as a barrier to their wider adoption and utility, urging the scientific community to explore strategies to enhance their mechanical robustness without compromising on their unique adaptive features.

In the realm of materials science, composite materials often pave the way for harnessing the best attributes of individual components to surmount their intrinsic limitations [18–22]. LCEs, despite their adaptability, suffer from the aforementioned mechanical constraints. One potential solution lies in the fabrication of LCEC materials, particularly by integrating reinforcing fibers such as carbon fiber. In our preceding research, we endeavored to amalgamate the properties of carbon fiber with LCE, giving birth to a carbon fiber reinforced liquid crystal elastomer [23]. The intent was clear: to leverage the inherent strength of carbon fiber,

thereby enhancing the mechanical properties of the LCE. However, challenges persisted. The rigidity introduced by carbon fiber proved to be a double-edged sword. It became evident that the preparation methodology was not without its pitfalls. Particularly, the inherent stiffness of the carbon fiber hindered optimal alignment, preventing the attainment of a  $0^\circ$  angle between the stretching direction and the orientation of the carbon fiber. As a result, while the mechanical attributes were significantly enhanced, the composite's ability to deform in line with the carbon fiber direction was curtailed. This posed a complex issue warranting additional investigation.

Advancements in material sciences have introduced the concept of 4D printing, where the fourth dimension represents the transformative ability of printed structures over time, usually interacting with environmental triggers [24–30]. This advanced printing technology permits the creation of transformable materials that can adapt and change post-production, making it a revolutionary tool for designing 'smart' structures [31–34]. Within the sphere of LCEs, 4D printing offers intriguing prospects, with research endeavors focused on harnessing the potential of LCEs to undergo controlled and programmable deformations post-printing [35–37]. Despite the success of these previous endeavors, the union of LCEs with rigid carbon fibers via 4D printing – a fusion that promises enhanced mechanical robustness while retaining LCE's unique deformation properties – has been largely unexplored. The potential of such a combination could propel the functionalities of LCEC to unprecedented levels, but the scientific community stands on the threshold, waiting for pioneering research in this direction.

The crux of this article pivots around an innovative approach to address the enduring challenges faced with LCEs and their mechanical constraints. We harness the capabilities of 4D printing to intertwine the transformability attributes of LCE with the strength of carbon fiber. By adopting this method, we introduced a pioneering structure, where LCE is seamlessly printed both below and above carbon fiber fabric. This resultant LCE-carbon fiber fabric-LCE sandwich composite is not just a manifestation of enhanced mechanical properties compared to pure materials, but it also furnishes a broader scope for deformation in LCECs (Figure 1a). Diverging from the traditional deformation designs of pure materials, our study goes a step further. By judiciously modifying the printing direction of LCE and its angular relationship with the carbon fiber direction, we've managed to engineer a spectrum of deformation methodologies. Our research determined that the presence of carbon fiber notably alters the deformation behavior of LCE when subjected to a consistent printing path. Specifically, we've achieved four distinct modes: bend, twist, wrap, and the intricate S-shape (Figure 1b). This article culminates with a quantitative investigation, probing into the nuanced relationship between LCEC deformation and the associated printing direction. Besides, our investigation rigorously engaged finite element analysis (FEA) to elucidate the bending strain energy discrepancies within the composite matrix, thereby furnishing a detailed comprehension of its mechanical behavior. This computational modeling substantiates our empirical observations and furnishes a robust predictive framework for engineering LCE composites with customized mechanical attributes and deformation profiles.

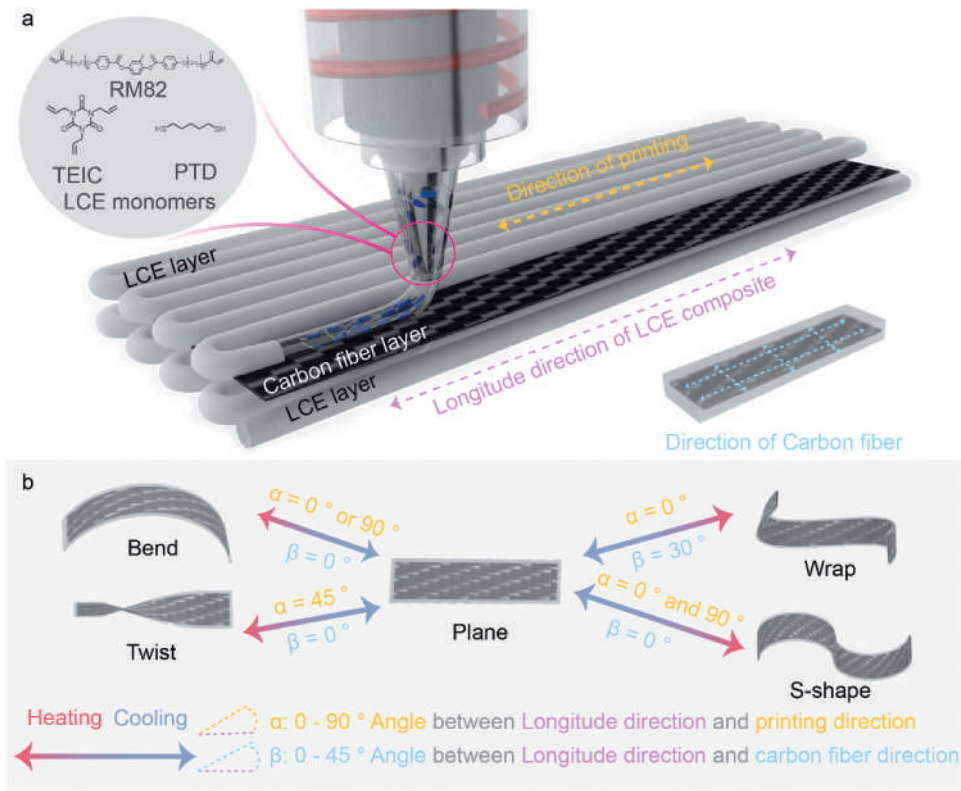


**Figure 1.** Illustration depicting: (a) the systematic fabrication procedure for LCEC; (b) diverse transformable geometries of LCEC based on variations in the  $\beta$  angle (ranging from  $0^\circ$  to  $45^\circ$ ) and the  $\alpha$  angle (extending from  $0^\circ$  to  $90^\circ$ ). The angle formed between the LCE printing trajectory and the longitudinal direction of the specimen is denoted as the  $\beta$  angle, while the angle between the orientation of the carbon fiber and the longitudinal direction of the specimen is labeled as the  $\alpha$  angle.

## 2. Experiment method

### 2.1. Materials

The liquid crystal acrylate RM82 (LC monomer) was procured from Jiangsu Hecheng Display Technology Co., Ltd (HCCH). The thiol chain extender, 1,5-pentanedithiol, the antioxidant butylhydroxytoluene (BHT), the photocuring agent (2-hydroxyethoxy)-2-methylpropiophenone (HHMP), and triethylamine were all produced by Sigma-Aldrich. The crosslinker utilized was Triallyl Isocyanurate (TAIC). Additionally, the carbon fiber fabric, characterized as Satin, 3K, with a weight of  $200 \text{ g m}^{-2}$  and thickness of 0.111 mm, was obtained from TORAY, Japan. All materials were commercially acquired.

### 2.2. Preparation of LCE oligomer

The RM82 (5.44 g), thiol chain extender (1.42 g), TAIC (0.51 g), antioxidant BHT (0.15 g), and photoinitiator HHMP (0.11 g) were combined in a 20 ml stainless steel cartridge. The monomers were introduced into the heating cartridge in powdered form and

subsequently subjected to heating at 90°C for a period of 30 minutes. Following thorough agitation, a uniformly distributed fluid mixture was obtained. Following this, triethylamine (0.07 g), was incorporated into the solution as catalyst. After blending for 30 seconds, the solution was subjected to a temperature of 60°C over a full day cycle to ensure through reaction between thiol and the acrylate. Upon completion of the reaction, a printable polydomain LC oligomer ink was procured.

### 2.3. Preparation of the LCECs

The LC oligomer ink was subsequently transferred to a high-temperature extruder printing head, an integrated component of the direct-ink printer (3D Bioplotter, EnvisionTEC). For the printing process, the ink was extruded at 65°C under a pressure of 2 bar and at a rate of 4 mm/s using a precision extrusion nozzle of 0.4 mm in diameter. Extrusion was oriented in varied directions atop the carbon fiber fabric. Post-printing, the liquid crystal elastomer (LCE) underwent a post-curing process under 365 nm ultraviolet (UV) radiation for duration about 20 minutes.

To create the LCEC, a sandwiched structure was employed. The foundational layer consisted of printed LCE, followed by a layer of carbon fiber fabric, with the subsequent third and fourth layers being printed LCE. We designate angle between the LCE printing route and sample's longitudinal axis as  $\alpha$  angle. Simultaneously, the orientation angle between the carbon fiber alignment and the longitudinal axis of the sample is referred to as the  $\beta$  angle.

Given that both the alignment of carbon fibers relative to the trajectory of deposition significantly influence mechanical testing outcomes, samples devoid of carbon fiber are labeled LCE0, LCE45, and LCE90, corresponding to  $\alpha$  angles of 0°, 45°, and 90° respectively. For samples embedded with carbon fiber fabric, nomenclature such as LCE0C0, LCE0C30, and LCE0C45 is employed, based on  $\beta$  angles of 0°, 30°, and 45° respectively. Herein, the numeral following LCE pertains to angle  $\alpha$ . In instances where mechanical testing isn't the focus, LCE0 is simplified to LCE and LCE0C0 to LCEC for clarity.

### 2.4. Characterizations

The specimens were analyzed using Utilizing a Perkin Elmer Spectrum Two FT-IR spectrometer, the attenuated total reflectance method was employed to produce FT-IR spectra. The sample's oriented structure was characterized by a 2D-WAXD analysis using the Xeuss 2.0 diffractometer system, equipped with a Pilatus 300K detector in Line Eraser configuration.

To assess mechanical attributes of the standard tensile samples, a dynamic testing apparatus with a 5 kN capacity sensor was utilized. These tensile evaluations were executed at a stretching velocity of 2 mm per second in a standard room temperature environment. Dynamic mechanical analysis (DMA) and thermal strain test were conducted by DMA Q800 from TA Assessments. The thermal transitions were analyzed by DSC 1 STAR Device from Mettler-Toledo, were carried out in a nitrogen atmosphere. During these measurements, the samples were initially elevated in temperature ranging from -30°C to 150°C and then back to -30°C at a steady rate of 10°C per minute.

Thermal stability of LCE samples was examined using thermogravimetric analysis (TGA), employing the TGA/DSC 1 STAR Device from Mettler-Toledo. In this evaluation, specimens were heated from room temperature up to 800°C at a uniform rate of 10°C per minute, all within an inert nitrogen atmosphere. The surface temperature profiles of the LCE actuators during operation were ascertained utilizing heat imaging technology provided by JENOPTIK InfraTec. Lastly, the transformational behaviors exhibited by the LCEC actuators were visually documented using a digital camera.

### 3. Results and discussion

We utilized the 4D printing methodology coupled with a two-step cross-linking approach for crafting the LCE. The initial formulation of the nematic oligomer inks integrated a combination of liquid crystal mesogens and an isotropic dithiol, specifically 1,5-pentanedithiol. This combination promoted the thiol-acrylate Michael addition reaction, resulting in a printable ink formulation. During the printing phase, the ink, which contained non-crosslinked liquid crystal oligomers, was pre-heated to 65°C to ensure optimal viscosity for extrusion. This ink was then dispensed through the nozzle of a direct-ink printing device (3D Bioplotter, EnvisionTEC). Notably, nematic inks possessing thiol terminations are suitable for direct printing. This printing method strategically programs the mesogen alignment orientation in conjunction with the print pathway due to the shear forces exerted.

Upon completing the deposition of the liquid crystal oligomer, the carbon fiber fabric is meticulously positioned atop the first layer, set at distinct  $\beta$  angles, ensuring direct contact with the underlying liquid crystal oligomer layer. Following this, the ink underwent a photo-crosslinking process, facilitated by the reaction between the thiol-terminated liquid crystal oligomer and the trifunctional vinyl cross-linker, TAIC. This process led to the curing of the LC oligomer, forming an LCE with the carbon fiber fabric adhered. The procedure is finalized by printing the subsequent second and third liquid crystal oligomer layers atop the carbon fiber, followed by a similar curing method.

#### 3.1. Spectra analysis

In this investigation, we conducted spectroscopic analyses to elucidate the progression of the chemical reaction inherent to the polymer's formation. We employed Fourier Transform Infrared Spectroscopy (FTIR) as a methodological approach to identify specific molecular groups within the polymer structure. Notably, across all examined samples, the molecular group associated with acrylate, which initially manifested a peak at 813  $\text{cm}^{-1}$ , disappeared post the thiol-acrylate reaction (as depicted in [Figure 2a](#)). This data strongly suggests that RM82 underwent a complete reaction with the thiol group subsequent to catalysis.

#### 3.2. Thermo properties

In our research, Both DSC and TGA techniques were applied to provide a detailed assessment of the thermal attributes of both LCE and LCEC. According to the DSC findings, the glass transition temperature for LCE was identified at approximately  $-9.01^\circ\text{C}$ , whereas for

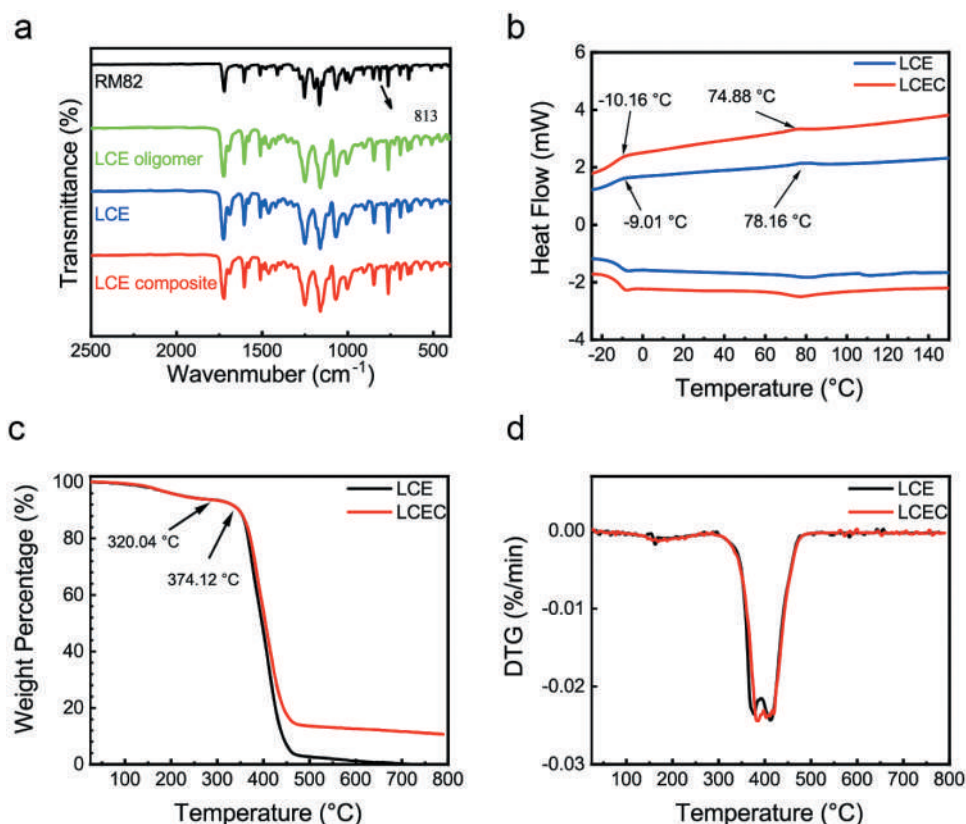


**Figure 2.** (a) FTIR results for LCE and LCEC synthesized through the thiol-acrylate reaction; (b) DSC results for LCEC specimens; (c) TGA results for LCEC specimens under a nitrogen atmosphere; (d) corresponding DTA curves for LCEC samples under a nitrogen atmosphere.

LCEC, it was discerned at around  $-10.16^{\circ}\text{C}$ . Moreover, the DSC analyses revealed establishing the transition temperature ( $T_{\text{NI}}$ ) from nematic to isotropic phases in the LCE as  $78.16^{\circ}\text{C}$  and that of LCEC to be  $74.88^{\circ}\text{C}$  (refer to Figure 2b). This observed variation is postulated to stem from specific interactions between the carbon fiber and the LCE matrix, suggesting that the incorporation of carbon fiber might influence the heat absorption capacity of the material.

Upon conducting the TGA assessment, the onset decomposition temperature for both LCE and LCEC was recorded at  $320.04^{\circ}\text{C}$ , with a peak decomposition rate temperature at  $374.12^{\circ}\text{C}$  (as shown in Figure 2c). The Differential Thermal Analysis (DTA) curve indicated that while the thermal decomposition rates of LCEC and LCE exhibited marginal disparities around  $400^{\circ}\text{C}$ , the overarching trend remained consistent (illustrated in Figure 2d). Such observations lead to the hypothesis that the amalgamation of carbon fiber and LCE potentially modulates the crystallization properties of the composite material.

### 3.3. Anisotropic characterization

We evaluated alterations in the liquid crystal order using 2D-WAXD experiments on samples maintained at ambient conditions. The resultant Debye ring patterns, derived



from the 2D-WAXD analyses, provided insights into the sample orientation at the microscopic scale. Given the potential influence of unidirectional carbon fibers on the Debye rings discerned through 2D-XRD, both LCE and LCEC exhibited peaks characterized by specific widths at  $2\theta = 19.63^\circ$  and  $2\theta = 20.85^\circ$  (refer to Figure 3a), corresponding to d-spacings of 4.51 Å and 4.25 Å, respectively. Moreover, LCEC showcased a pronounced peak at  $2\theta = 2.46^\circ$ , translating to a d-space of 35.87 Å, a feature not discernible in LCE. Thus, it is hypothesized that this distinct peak might be indicative of carbon fiber integration. Upon azimuthal integration, the peak position of LCE prominently appeared at  $88^\circ$ , whereas LCEC manifested clear peak positions at  $178^\circ$  (refer to Figure 3b). The additional peaks in the azimuthal angle of LCEC can be attributed to the utilization of carbon fiber fabric with dual fiber orientations. A visual comparison can be made between Figures 3c and 3d. The absence of carbon fibers in the LCE depicted in Figure 3c is evident, given the lack of a cross pattern at its center. Conversely, the presence of carbon fibers in Figure 3d introduces a distinctive cross pattern centrally. These observations suggest that, aside from the carbon fiber component, LCE and LCEC possess similar orientation distributions. While the carbon fiber introduces certain modifications to the orientation distribution of the LCE matrix, these alterations are subtle.

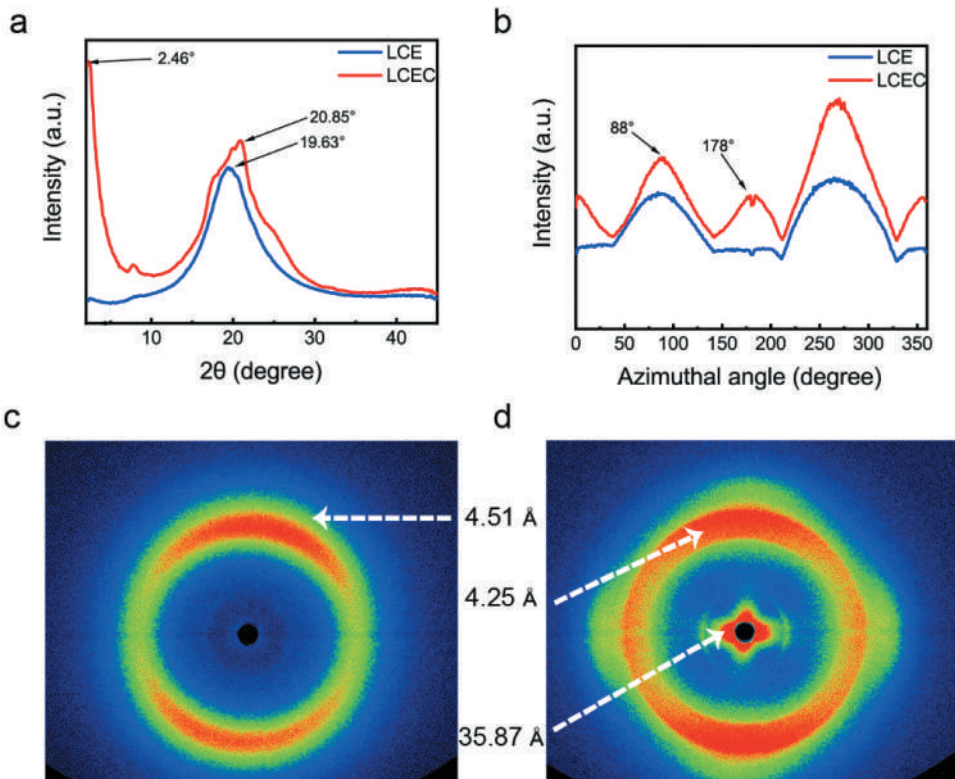


**Figure 3.** 2D-WAXD characterization of LCE samples: (a) WAXD curves for LCEC samples showcasing peaks at  $2\theta = 2.5^\circ$ ,  $2\theta = 19^\circ$ , and  $2\theta = 20^\circ$ . Utilizing the equation  $\lambda = 2d \sin \theta$  (where  $\lambda = 1.54 \text{ \AA}$ ), the calculated d-spacings are 35 Å, 4.51 Å, and 4.25 Å, respectively; (b) Azimuthal angle representations for LCEC specimens; (c) debye ring patterns for LCE; (d) debye ring patterns for LCEC.

### 3.4. Mechanical property and micro structure characterization

In our comprehensive study to ascertain the mechanical properties of the LCEC, we fabricated an array of samples by modulating the  $\alpha$  and  $\beta$  angles. These were designated as LCE0, LCE45, LCE90, LCE0C0, LCE0C30, and LCE0C45. For clarity, the initial numeral in each sample's designation pertains to the  $\alpha$  angle, while the subsequent denotes the  $\beta$  angle. An omission of the latter numeral indicates that the sample comprises the pure material.

Upon tensile testing, we observed a diverse range of outcomes. The documented yield strengths for LCE0, LCE45, LCE90, LCE0C0, LCE0C30, and LCE0C45 were 0.53 MPa, 0.04 MPa, 0.21 MPa, 4.59 MPa, 3.89 MPa, and 1.57 MPa, respectively. Simultaneously, their respective maximum fracture strains were recorded as 489.68%, 1912.02%, 1060.24%, 18.28%, 24.60%, and 44.91% (refer to Figures 4a and 4b). A consolidated dataset is provided in Table S1.

These results distinctly demonstrate that the integration of carbon fiber into the LCEC significantly enhances its mechanical resilience. Notably, the augmentation is most pronounced when the carbon fiber is oriented at a  $0^\circ$  relative to the LCE. Conversely, an angle of  $45^\circ$  between the carbon fiber and LCE results in the least reinforcement. Such empirical data emphatically underscore the advantages of utilizing 4D printing to merge carbon fiber with LCE, refining their mechanical traits.

Additionally, an exceptional result was identified for LCE45, which demonstrated a notably elevated fracture strain – an observation not reported in previous literature. Our analytical interpretation suggests that prior to deformation, LCE45 experiences an initial rotational movement during stretching. Another significant observation pertained to the fracture strain of LCE90, which was approximately double that of LCE0.

To gain a deeper understanding at the microstructural level, Scanning Electron Microscopy (SEM) was employed for LCEC characterization. Our examination revealed that the carbon fiber exhibited a diameter nearing 7 microns, whereas the LCE had a diameter approximately 500 microns. The SEM imagery evidences a favorable bond between the carbon fiber and LCE (as illustrated in Figure S1).

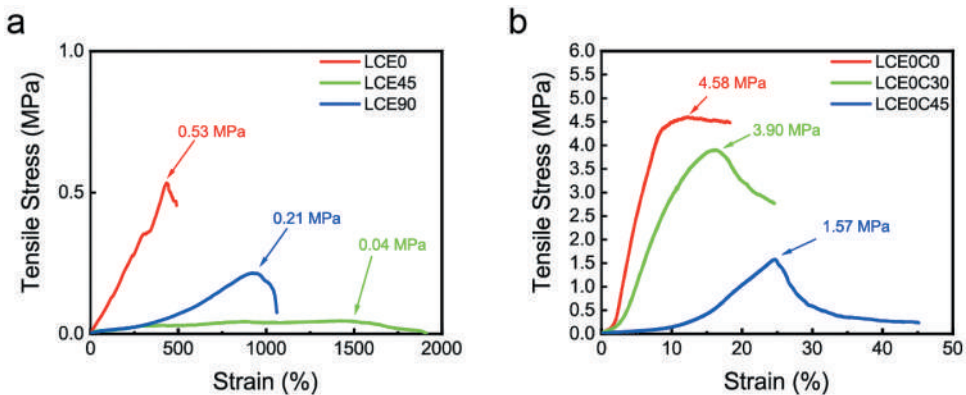


**Figure 4.** Tensile test of (a) LCE and (b) LCEC specimens across varied fiber orientations and printing trajectories.

### 3.5. Reversible transformation upon changing the $\alpha$ direction

Subsequent experimental endeavors aimed to determine the reversible deformation capabilities of various LCEC samples. A principal objective was to validate the proposition that the LCEC combination retains the intrinsic reversible deformation ability of LCE while simultaneously fortifying its mechanical properties. By comparing the deformation behaviors of LCEC to pure LCE, this investigation aimed to elucidate the differences between the two. The outcomes of these experiments are illustrated in [Figures 5a and 5b](#).

When the samples were subjected to a heating protocol of 140°C and subsequently cooled to ambient conditions, their reversible deformation metrics were systematically recorded. For both the LCE0 and LCE0C0 samples (refer to [Figures 5ai and 5bi](#)), each displayed characteristics of reversible deformation. However, there was a pronounced difference in the amplitude of their bending angles. The unadulterated LCE0 exhibited a comprehensive 166.99° bending range (Figure S2), while its composite counterpart, LCE0C0, achieved only 89.21° range (Figure S3). This diminished deformation in the LCE0C0 sample is ascribed to the inherent stiffness of the carbon fiber, which counteracts the extensive deformation tendencies of the LCE.

The samples LCE45 and LCE45C0 (refer to [Figures 5aii and 5bii](#)) exhibited unique deformation patterns. Specifically, LCE45 exhibited a torsional deformation with an angular displacement of 90°. In contrast, LCE45C0 presented a reduced torsional capability, evidenced by a twist angle of merely 30°. The primary reason for this reduction in torsional movement is attributed to the restrictive behavior of the carbon fibers during torsion. Additionally, post-torsion, LCE45C0 displayed an irreversible deflection deformation, a deviation not evident in its non-composite counterpart. This behavior was interpreted as the carbon fibers' inability to seamlessly navigate the predefined deformation trajectory designated for the LCE. Strengthening the interconnection between the LCE and carbon fiber is anticipated as a potential approach to rectify this irregularity.

The deformation repertoire was further diversified with the introduction of the LCE90 and LCE90C0 samples (refer to [Figures 5aiii and 5biii](#)). The deformation behavior of LCE90 mirrored that of LCE0 but interestingly demonstrated an opposing directional bending, attributable to the distinct printing path. The bending angle persisted at 166.99°. Conversely, LCE90C0's deformation pattern was distinct. While LCE0 arched upwards at its peripheries, LCE90C0 manifested an upward curvature centrally, spanning 79.61°. Upon analysis, it was discerned that the rod-like structure of the carbon fibers, due to their intrinsic rigidity, resisted deformation, particularly when curtailed in length. As a result, the carbon fibers obstruct LCE deformation along the shorter axis, directing it longitudinally, leading to the observed bending characteristic of LCE90C0. Notably, this deformation model represents a pioneering observation, not identified in previous studies. For detailed visualization of the specific deformation processes mentioned, please refer to Supplementary Videos S1 to S6.

### 3.6. Reversible transformation upon changing the $\beta$ direction

Broadening the scope of analysis to consider the impact of the  $\beta$  angle, a systematic study was initiated to ascertain its influence on the deformation characteristics of LCEC samples, as depicted in [Figure 6](#) and Video S9 to S11. Three distinct samples were

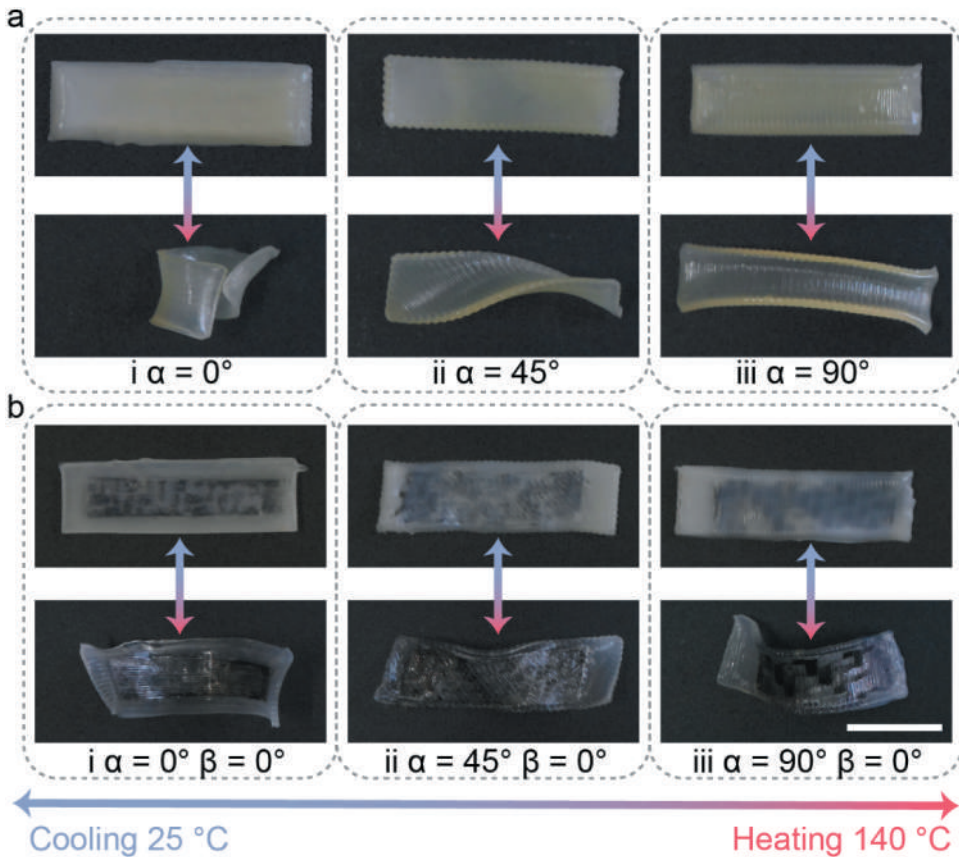


**Figure 5.** Transformation behaviors of LCE and LCEC based on distinct  $\beta$  and  $\alpha$  angles, influencing bending and twisting deformations. (a) In pure LCE, deformation aligns with the printing direction, depicting: (i)  $\alpha = 0^\circ$  as bending along the longitudinal axis, (ii)  $\alpha = 45^\circ$  as twisting, (iii)  $\alpha = 90^\circ$  as bending across the transverse axis. (b) With the carbon fiber composite material, transformations for (i)  $\alpha = 0^\circ \beta = 0^\circ$  and (ii)  $\alpha = 45^\circ \beta = 0^\circ$  parallel pure LCE, albeit with subdued transformation. However, for (iii)  $\alpha = 90^\circ \beta = 0^\circ$ , the sample exhibits a reverse bending trend compared to (i). Scale bar indicates 15 mm.

selected for this investigation: LCE0C30, LCE90C30, and LCE90C45. The resultant data yielded several noteworthy findings. Both LCE0C30 and LCE90C30 displayed torsional deformations overlaid on their primary bending, a behavior termed as the ‘wrap structure’ (refer to Figures 6i and 6ii). This deformation pattern is postulated to arise from the LCE’s propensity to deform in alignment with the carbon fiber’s orientation, a consequence of the deflective forces exerted by the latter. Specifically, LCE0C30 exhibited a pitch of 6 mm accompanied by a bending angle of  $20.12^\circ$ , whereas LCE0C90 presented a pitch of 10 mm coupled with a bending angle of  $70.61^\circ$ . In congruence with earlier deductions, the bending paths of LCE0C30 and LCE90C30 were diametrically opposed. However, their bending angles varied substantially. LCE90C30 showcased a marked  $70.61^\circ$  bend, significantly surpassing the more restrained  $20.12^\circ$  angle of LCE0C30. These observations provide valuable perspectives for refining LCE actuator designs to meet distinct deformation requirements.

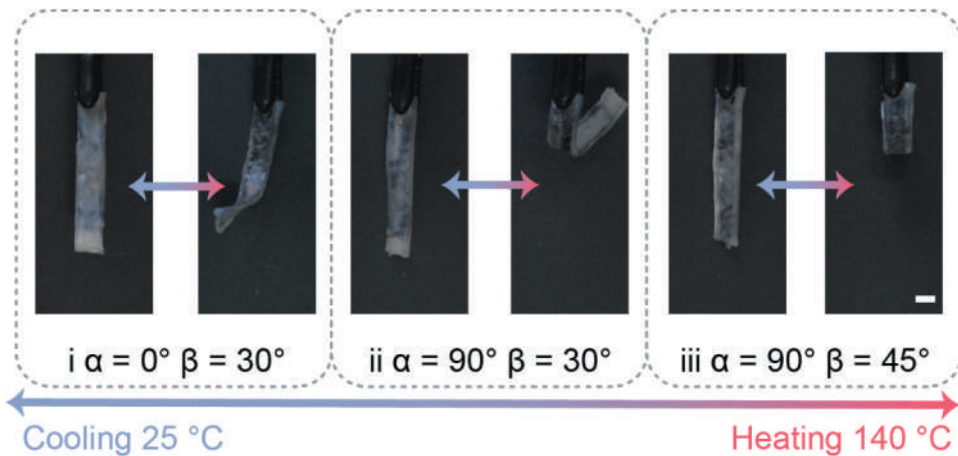


**Figure 6.** Transformation behaviors of LCEC governed by varied  $\beta$  and  $\alpha$  angles. Based on these angles, specimens demonstrate a wrapping transformation. With angles (i)  $\alpha = 0^\circ$  and (ii)  $\alpha = 90^\circ$ , samples bend and deform in opposite directions, whereas (iii) at  $\beta = 45^\circ$ , the wrapping phenomenon is absent, showcasing solely the longitudinal bending action of the sample. Scale bar indicates 5 mm.

Concerning LCE90C45, no unique wrap structure was discerned. Instead, it exhibited a standard deformation similar to LCE0, presenting a bending angle of  $82.15^\circ$  (Figures 6iii).

### 3.7. Crafting complex geometries

Beyond the aforementioned observations, there is an ambition to fabricate more intricate deformational shapes, thereby highlighting the distinctions between LCE and LCEC. Guided by the revelations from previous experiments, an initiative was undertaken to design LCECs capable of adopting an 'S' configuration. The paramount consideration was to ensure that LCE components on antipodal surfaces exhibited counteractive deformation directions.

**Approach I:** By capitalizing on the contrasting bending paths of LCE0C0 and LCE90C0, a dualistic printing strategy was employed. A layer of carbon fiber was incorporated, and disparate printing techniques were utilized for each side of this carbon fiber layer. The left section of the specimen was characterized by LCE90C0, whereas the right section was patterned with LCE0C0. The crafted LCEC exhibited an adeptness in achieving an S-shaped deformation (refer to Figure 7a and Supplementary Video S10).

**Approach II:** A sophisticated methodology involved staggered layering of carbon fiber fabric upon a base printed with LCE0. The fabrication process began with establishing the foundational layer and the left portion of LCE. This foundation was then overlaid with a continuous expanse of carbon fiber fabric. Ensuing layers of LCE were successively added, culminating with a terminal layer. The final configuration of the carbon fiber was evocative of Figure 7b and Supplementary Video S11. This elaborate design strategy also produced samples adept at S-shaped deformation upon thermal activation.

In an endeavor to visually elucidate the deformational distinctions between LCE and LCEC, an elaborate floral design was realized through 3D printing. The floral construct was

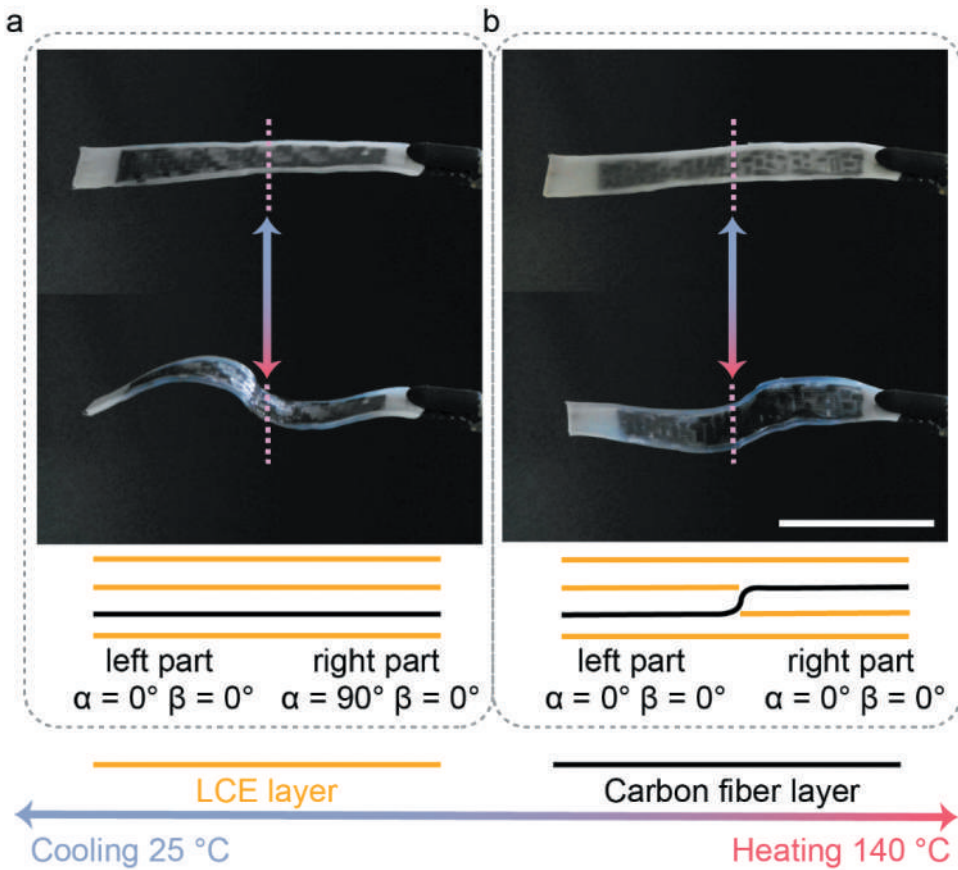


**Figure 7.** Reversible transformations in LCEC yielding an 'S' shape. (a) Different printing directions are employed for the left ( $\alpha = 0^\circ$ ) and right ( $\alpha = 90^\circ$ ) segments of the specimen; (b) both left and right segments follow the same printing trajectory ( $\alpha = 90^\circ$ ), but differ in the carbon fiber fabric layering. Scale bar signifies 20 mm.

bifurcated, with one hemisphere representing LCE and the opposing one showcasing LCEC. This illustrative embodiment poignantly emphasized the deformational disparities inherent between the two entities (as illustrated in Figure 8, along with Supplementary Video S12 and S13).

### 3.8. Finite Element Analysis of LCEC

To elucidate the deformation mechanism of the LCEC, finite element analysis was employed for the simulation of its deformation process utilizing the ABAQUS software. Based on the DMA and expansion rate data for LCE provided by Figure 9a, it is evident that LCE's properties are temperature-dependent, with both its stiffness and inherent shape being contingent upon changing temperatures. The modulus of elasticity of the LCE exhibits a piecewise linear relationship before and after its transformation.

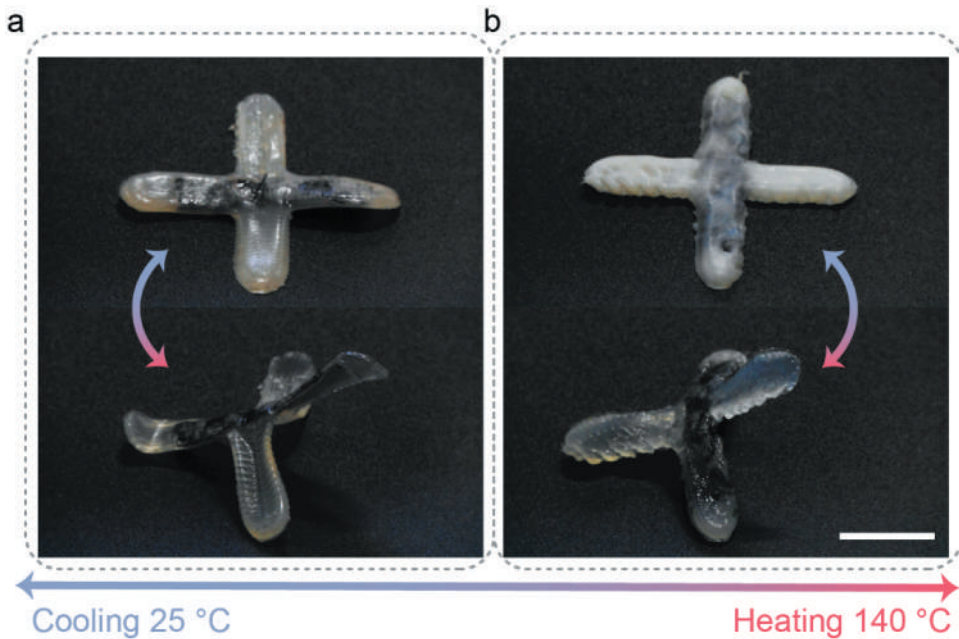


**Figure 8.** Reversible transformations of LCEC crafting a floral design. Each flower blends pure materials vertically and composite materials horizontally: (a) upper segment:  $\alpha = 0^\circ$ ; lower segment:  $\alpha = 90^\circ$ ; left segment:  $\alpha = 90^\circ$  and  $\beta = 45^\circ$ ; right segment:  $\alpha = 0^\circ$  and  $\beta = 45^\circ$ ; (b) upper segment:  $\alpha = 45^\circ$  and  $\beta = 0^\circ$ ; lower segment:  $\alpha = 135^\circ$  and  $\beta = 0^\circ$ ; left segment:  $\alpha = 135^\circ$ ; right segment:  $\alpha = 45^\circ$ . Scale bar represents 15 mm.

Consequently, this study employs a piecewise linear function to approximate the temperature-dependent Young's modulus of LCE.

$$E = \begin{cases} 6.829 \times 10^{-3} + 0.0239T, & T \leq 70^\circ\text{C} \\ 0.767 - 0.00232T, & T > 70^\circ\text{C} \end{cases}$$

where the unit of temperature is Celsius, and the unit of Young's modulus is MPa. In our implementation, subroutine is not used. In the practical configuration, Young's modulus is piecewise linearly fitted to the experimental data using the least squares method. Utilizing the data thus specified, ABAQUS directly provided the corresponding temperature-modulus linear fitting curve. Building on this information, the deformation of the material was further simulated.

As delineated in the temperature-contraction curve for LCE in [Figure 9b](#), the contraction strain of LCE exhibits a near-linear correlation with temperature during the cooling process. To characterize the anisotropic temperature-dependent deformation behavior of LCE, this modeling employs a transverse isotropic expansion hypothesis. This model elucidates the thermally reversible contraction characteristics of LCE materials. To comprehensively understand the deformation mechanism of LCE, it is crucial to recognize that its shape deformation markedly surpasses its volume deformation. Consequently, for the sake of this study, LCE is considered an incompressible material, eliminating the need to ascertain its thermal expansion rate. Based on the linear regression analysis of the temperature-contraction curve, the expansion coefficient in the printing direction is

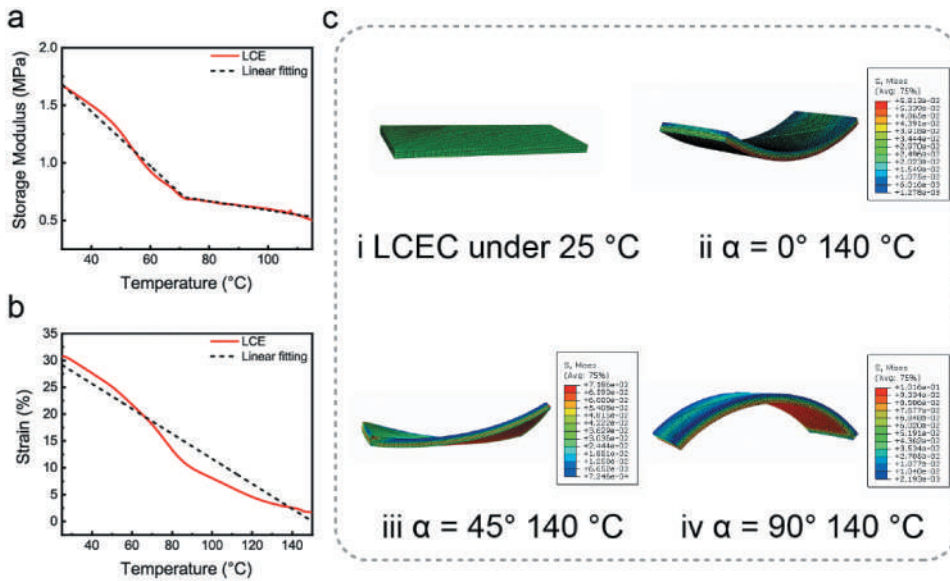


**Figure 9.** Results from FEA modeling illustrate stress distributions across various LCEC actuator configurations: (a) DMA and linear fitting result of LCE; (b) contraction strain of LCE depending on different temperature; (c) i LCEC at ambient temperature; ii LCEC exhibiting bending deformation for the configuration  $\alpha = 0^\circ$ ; iii LCEC displaying twisting deformation under the configuration  $\alpha = 45^\circ$ ; iv LCEC presenting bending deformation in the opposite direction for the configuration  $\alpha = 90^\circ$ , in contrast to the configuration  $\alpha = 0^\circ$ .

denoted as  $\alpha_1 = -0.235\%$ , and the expansion coefficients orthogonal to the printing direction are  $\alpha_2$  and  $\alpha_3$ , both equating to  $0.1175\%$  obtained by the incompressibility.

Three distinct LCEC variants, differentiated by their printing paths as depicted in Figure 5b, were modeled to forecast their deformation behaviors. The specified geometrical dimensions of these LCEC variants are  $30 \text{ mm} \times 12 \text{ mm} \times 1.2 \text{ mm}$ . Sequentially printed from the base upwards, three LCE layers are incorporated, with the carbon fiber situated between the first and the second layers. Within the finite element model, the LCE instances is segmented into hexahedral elements, each measuring  $0.2 \text{ mm} \times 0.2 \text{ mm} \times 0.2 \text{ mm}$ , and the aforementioned LCE material constitutive model is applied. Dependent on the printing trajectory, material coordinate system rotations of  $0^\circ$ ,  $45^\circ$ , and  $90^\circ$  are conferred on the LCE matrix in alignment with the path orientation. Given the absence of discernible debonding or deterioration at the juncture between the carbon fiber reinforcement and the LCE substrate during experimental observations, the carbon fiber layer is meshed into  $0.2 \text{ mm} \times 0.2 \text{ mm}$  shell elements and tied to each node at a height of  $0.4 \text{ mm}$  of the LCE instances. This ensures a compatible deformation between the LCE matrix and the carbon fiber layer.

The insights from the finite element simulations are depicted in Figure 9c. Notably, symmetrical bending deformation is observable when  $\alpha = 0^\circ$  and  $\alpha = 90^\circ$ , while torsional deformation emerges when  $\alpha = 45^\circ$ . The calculation results indicate that the experimental and simulation results are consistent. Stress analysis elucidates that the carbon fiber layer predominantly resists in-plane stress, thereby constraining the contraction deformation of



LCE neighboring the carbon fiber layer. However, the layer offers minimal resistance to bending, facilitating the simultaneous realization of substantial tensile stiffness and pronounced bending deformation in the LCEC. The underlying mechanism for LCEC's bending deformation emanates from the carbon fiber layer's constraint on the LCE matrix's deformation. Consequently, the entire sample undergoes strain compatibility across its thickness to minimize energy expenditure. Additionally, it merits attention that in instances where  $\alpha = 90^\circ$ , the LCEC sample's bending is aligned with the long axis rather than the short one. This alignment is attributed to the reduced overall bending strain energy associated with bending along the lengthier axis. The findings from the finite element analysis reaffirm this experimental observation.

## 4. Conclusions

In the pursuit of advancing material science, our research leveraged 4D printing methodologies to examine the intricate relationship between LCE and carbon fiber fabric. Our primary objective centered on enhancing the mechanical properties of LCEC, aiming for a harmonious integration of carbon fiber's robustness with LCE's adaptability. A notable discovery was the augmentation of LCE's tensile strength by eight times upon amalgamation with carbon fiber fabric. Moreover, distinct deformation patterns emerged across various LCEC configurations, such as bending, twisting, wrapping, and forming an S-shape. It was discerned that the orientation of carbon fibers can radically alter the deformational outcomes, even under identical printing trajectories. To elucidate the intricacies of LCEC deformation, we employed the ABAQUS software for finite element analysis, delving into the impact of carbon fiber on the LCE framework and elucidating the bending deformation mechanism inherent to LCEC. The synthesis of our experimental and simulation findings provides crucial guidelines for the development of high-strength LCECs exhibiting diverse deformation patterns.

## Disclosure statement

No potential conflict of interest was reported by the author(s).

## Funding

The work was supported by the National Key R&D Program of China [2022YFB3805700].

## ORCID

Jinsong Leng  <http://orcid.org/0000-0001-5098-9871>

## Supporting information

Supporting Information is available from the author.

## References

- [1] Ware TH, McConney ME, Wie JJ, et al. Voxelated liquid crystal elastomers. *Science*. 2015;347(6225):982–984.
- [2] White TJ, Broer DJ Programmable and adaptive mechanics with liquid crystal polymer networks and elastomers. *Nat Mater*. 2015;1087(11):1087–1098.
- [3] Wang Y, Dang A, Zhang Z, et al. Repeatable and reprogrammable shape morphing from photoresponsive gold nanorod/liquid crystal elastomers. *Adv Mater*. 2020;32(46):2004270.
- [4] Wang M, Hu X-B, Zuo B, et al. Liquid crystal elastomer actuator with serpentine locomotion. *Chem Commun*. 2020;56(55):7597. doi: 10.1039/D0CC02823A
- [5] Kaspar C, Ravoo BJ, van der Wiel WG, et al. The rise of intelligent matter. *Nature*. 2021;594:345.
- [6] Wang Y, Liu J, Yang S. Multi-functional liquid crystal elastomer composites. *Appl Phys Rev*. 2022;9:011301.
- [7] Zhao J, Zhang L, Hu J, Varied alignment methods and versatile actuations for liquid crystal elastomers: A review. *Adv Intell Syst*. 2022; 4(3):2100065.
- [8] Aburaya Y, Na H, Orihara H, et al. Electric-field-induced deformation of a chiral liquid-crystal elastomer in smectic A phase. *Korea-Aust Rheol J*. 2012;24:83.
- [9] He Q, Wang Z, Wang Y, et al. Electrically controlled liquid crystal elastomer-based soft tubular actuator with multimodal actuation. *Sci Adv*. 2019;5:eaax5746.
- [10] Zhang J, Guo Y, Hu W, et al. Liquid crystal elastomer-based magnetic composite films for reconfigurable shape-morphing soft miniature machines. *Adv Mater*. 2021;33:2006191.
- [11] Fowler HE, Rothmund P, Keplinger C, et al. Liquid crystal elastomers with enhanced directional actuation to electric fields. *Adv Mater*. 2021;33:2103806.
- [12] Li Y, Yu H, Yu K, et al. Reconfigurable three-dimensional mesostructures of spatially programmed liquid crystal elastomers and their ferromagnetic composites. *Adv Funct Mater*. 2021;31:2100338.
- [13] Song X, Zhang W, Liu H, et al. 3D printing of liquid crystal elastomers-based actuator for an inchworm-inspired crawling soft robot. *Front Robot AI*. 2022 ;9:889848.
- [14] Yang M, Xu Y, Zhang X, et al. Bioinspired phototropic MXene-reinforced soft tubular actuators for omnidirectional light-tracking and adaptive photovoltaics. *Adv Funct Mater*. 2022;32:2201884.
- [15] Chen M, Gao M, Bai L, et al. Recent advances in 4D printing of liquid crystal elastomers. *Adv Mater*. 2023;35:2209566.
- [16] Wang Y, Yin R, Jin L, et al. 3D-printed photoresponsive liquid crystal elastomer composites for free-form actuation. *Adv Funct Mater*. 2023;33:2210614.
- [17] Xiao Y-Y, Jiang Z-C, Tong X, et al. Biomimetic locomotion of electrically powered “Janus” soft robots using a liquid crystal polymer. *Adv Mater*. 2019;31:1903452.
- [18] Yang L, Setyowati K, Li A, et al. Reversible infrared actuation of carbon nanotube-liquid crystalline elastomer nanocomposites. *Adv Mater*. 2008;20:2271.
- [19] Li C, Liu Y, Lo C-W, et al. Reversible white-light actuation of carbon nanotube incorporated liquid crystalline elastomer nanocomposites. *Soft Matter*. 2011;7:7511.
- [20] Yao L, Yan H, He Y, et al. Actuation performances of catkin fibers reinforced thiol-acrylate main-chain liquid crystalline elastomer. *Int J Smart Nano Mater*. 2022;13:668.
- [21] Yang Y, Wang Y, Yao T, et al. A flexible and smart shape memory alloy composite sheet based on efficient and bidirectional thermal management. *Int J Smart Nano Mater*. 2022;13:315.
- [22] Liu X, Ji H, Liu B, et al. All-solid-state carbon-nanotubefiber-based finger-muscle and robotic gripper. *Int J Smart Nano Mater*. 2022;13:64.
- [23] Xia Y, Mu T, He Y, et al. Fiber-reinforced liquid crystalline elastomer composite actuators with multi-stimulus response properties and multi-directional morphing capabilities. *Compos B Eng*. 2023;256:110640.
- [24] Ambulo CP, Ford MJ, Searles K, et al. 4D-printable liquid metal-liquid crystal elastomer composites. *ACS Appl Mater Interfaces*. 2021;13:12805.
- [25] Zhai F, Feng Y, Li Z, et al. 4D-printed untethered self-propelling soft robot with tactile perception: rolling, racing, and exploring. *Matter*. 2021;4:3313.

- [26] Peng X, Wu S, Sun X, et al. 4D printing of freestanding liquid crystal elastomers via hybrid additive manufacturing, *Adv Mater.* **2022**;34(39):2204890.
- [27] Zhao W, Zhu J, Liu L, et al. A bio-inspired 3D metamaterials with chirality and anti-chirality topology fabricated by 4D printing. *Int J Smart Nano Mater.* **2023**;14:1.
- [28] Yang X, Valenzuela C, Zhang X, et al. Robust integration of polymerizable perovskite quantum dots with responsive polymers enables 4D-printed self-deployable information display. *Matter.* **2023**;6:1278.
- [29] Lu X, Ambulo CP, Wang S, et al. 4D-printing of photoswitchable actuators. *Angew Chem Int Ed.* **2021**;60:5536.
- [30] Zhang W, Wang H, Wang H, et al. Structural multi-colour invisible inks with submicron 4D printing of shape memory polymers. *Nat Commun.* **2021**;12:112.
- [31] Zhang F, Wen N, Wang L, et al. Design of 4D printed shape-changing tracheal stent and remote controlling actuation. *Int J Smart Nano Mater.* **2021**;12:375.
- [32] Zhang Z, Demir KG, Gu GX. Developments in 4D-printing: a review on current smart materials, technologies, and applications. *Int J Smart Nano Mater.* **2019**;10:205.
- [33] Khalid MY, Arif ZU, Tariq A, et al. *Eur. Polym J.* **2024**;205:112718.
- [34] Arif ZU, Khalid MY, Tariq A, et al. 3D printing of stimuli-responsive hydrogel materials: literature review and emerging applications. *Giant.* **2023**;17:100209.
- [35] Saed MO, Ambulo CP, Kim H, et al. Molecularly-engineered, 4D-Printed liquid crystal elastomer actuators *Adv Funct Mater.* **2019**;29:1806412.
- [36] Mistry D, Traugott NA, Sanborn B, et al. Soft elasticity optimises dissipation in 3D-printed liquid crystal elastomers. *Nat Commun.* **2021**;12:6677.
- [37] Wallin TJ, Pikul J, Shepherd RF. 3D printing of soft robotic systems *Nat Rev Mater.* **2018**;3:84.